Supporting Information

An Acentric 3-D Metal-Organic Framework with Threefold Interpenetrated Diamondoid Network: Second-Harmonic-Generation Response, Potential Ferroelectric Property and Photoluminescence

Wei-Wei Zhou,[a] Bo Wei,[b] Feng-Wu Wang,[a] Wen-Yan Fang,[a] Dao-Fu Liu,[a] Yi-Jun Wei,[a] Mai Xu[a], Xing Zhao[a] and Wang Zhao*[a]

[a] *Anhui Key Laboratory of Low Temperature Co-fired Materials, College of Chemistry & Materials Engineering, Huainan Normal University, Huainan, Anhui 232038, PR China. E-mail: wzhao@hnnu.edu.cn; Tel: +86 5546862556.*

[b] *School of Chemistry and Materials Engineering, Jiangsu key Laboratory of Advanced Functional Materials, Changshu Institute of Technology, Changshu, Jiangsu 215500, PR China.*

1. Materials

All reagents were purchased commercially and used without further purification.

2. Determination

The FT-IR spectrum was recorded on a Nicolet Magna 750 FT-IR spectrophotometer in the region of 4000–400 cm^{-1} using KBr pellets as bases. Elements analyses of C, H and N were carried out with an Elementar Vario MICRO. The TG/DTA curve of **1** was measured on TA Q600 under a N_2 atmosphere with a ramp rate of 10 K/min.

The solid-state photoluminescent determinations were performed on F-4600 (excitation and emission slits, 2.5 nm; data interval, 0.2 nm and scan speed, 1200 nm/min). The quantum yield was measured on an Edinburgh FLS920 fluorescence spectrometer equipped with an optical integrating sphere.

The UV-vis spectrum was recorded at room temperature on computer-controlled PE Lambda 900 UV-vis spectrometer equipped with an integrating sphere in the

wavelength range 200–2000 nm. A $BaSO_4$ plate was used as a reference, on which finely ground powder of the sample was coated. The absorption spectrum was calculated from reflection spectra by the Kubelka-Munk function:[i] $\alpha/S = (1-R)^2/2R$, where α is the absorption coefficient, S is the scattering coefficient that is practically wavelength independent when the particle size is larger than 5 μm, and R is the reflectance. The band gap value was determined as the intersection point between the energy axis at the absorption offset and the line extrapolated from the linear portion of the absorption edge in the α/S versus E (eV) plot.

Powder X-ray diffraction (PXRD) pattern (at room temparature) was measured on a D8 Advance powder diffractometer at 40 kV and 40 mA using Cu-K_α (λ = 1.54056 Å), with a step size of 0.02 °. And PXRD (at 50-200 °C) was measured on a X' pert Pro powder diffractometer at 40 kV and 40 mA using Cu-K_α (λ = 1.54056 Å), with a step size of 0.02 °. The simulated powder pattern was calculated using single-crystal X-ray diffraction data and processed by the free Mercury v2.4 program provided by the Cambridge Crystallographic Data Centre.

The experimental method of Kurtz and Perry was used to measure powder SHG signals with a 1064-nm laser [ii]. Powder samples of **1** were prepared, and microcrystalline KDP was used as comparative standards. A pulsed Q-switched Nd:YAG laser at a wavelength of 1064 nm was used to generate the SHG signal. The backward scattered SHG light was collected using a spherical concave mirror and passed through a filter that transmits only 532 nm radiation. The dielectric constant (ε') and dielectric loss tangent (tanδ) were measured by a computer-controlled Alpha dielectric/impedance spectrometer (NovoControl). The measurements were performed as a function of temperature from 20 °C to 200 °C. The ferroelectric property of a pellet of powder sample was measured at an aixACCT TF Analyzer 2000 ferroelectric tester at room temperature as the sample was immersed in insulating oil.

3. X-ray crystallographic study

The single-crystal X-ray diffraction measurement of **1** was performed on Rigaku Mercury CCD (T = 293(2) K) diffractometer, respectively, using graphite

monochromated Mo-Kα radiation (λ = 0.71073 Å). Intensity data set was collected using the ω scan technique and corrected for Lp effects. The structure was solved by the direct method using the Siemens SHELXTLTM Version 5 package of crystallographic software.[iii] The difference Fourier maps based on these atomic positions yield the other non-hydrogen atoms. The structure was refined using a full-matrix least-squares refinement on F2. All non-hydrogen atoms were refined anisotropically. Hydrogen atoms were added according to the theoretical models.

4. Calculation of density of states (DOS)

The crystallographic data of **1** determined by X-ray was used to calculate its electronic structure. The calculation of electronic structure was performed with the CASTEP code based on the density functional theory (DFT) using a plane-wave expansion of the wave functions and norm-conserving pseudopotential. We used the generalized gradient approximation (GGA) in the scheme of Perdew-Burke-Eruzerhof (PBE) to describe the exchange and correlation potential.

5. Synthesis of 1:

A mixture of HL2 (111 mg, 0.8 mmol), $Cd(CH_3COO)_2 \cdot 2H_2O$ (92 mg, 0.4mmol), water (6 mL) and ethanol (3 mL) was loaded into a 25 mL Teflon-lined steel autoclave, and heated at 190 °C for 4 days, yielding colourless crystals of **1**. Yield: 50% (based on Cd). Anal. calcd (%): C, 35.10; H, 3.11; N, 13.64. Found: C, 35.15; H, 3.14; N, 13.59. IR data (KBr pellet): 3595 (m), 3522 (m), 3441 (s), 3338 (s), 3225 (s), 3070(m), 2592(w), 1911(w), 1653(s), 1539(vs), 1448(vs), 1404 (vs), 1344 (m), 1248(m), 1115 (w), 1049(w), 1005 (m), 955 (m), 899 (m), 827 (s), 773 (s), 704 (s), 631 (m), 569 (m), 538 (m), 438 (m). (Figure S1).

6. Crystal and structure refinement for 1:

$C_{36}H_{38}Cd_3N_{12}O_{16}$, *M*r = 1231.98, Trigonal, *R*3*c*, *a* = 24.0596(8), *c* = 13.2216(7) Å, *V* = 6628.1(5) Å^3, *T* = 293(2) K, *Z* = 6, ρ_{calcd} = 1.852 g/cm^3, μ =1.515 mm^{-1}. Final *R* indices [$I > 2\sigma(I)$], *R*1 = 0.0219, *wR*2 = 0.0466. GoF on F2 = 1.058. CCDC-

1419893.

Table S1

Crystal Data and Structure Refinement for **1**.

chemical formula	$C_{36}H_{38}Cd_3N_{12}O_{16}$
fw	1231.98
cryst size (mm^3)	0.20 × 0.04 × 0.03
cryst syst	Trigonal
space group	*R3c*
a (Å)	24.0596(8)
c (Å)	13.2216(7)
V ($Å^3$)	6628.1(5)
Z	6
D_{calcd} (g cm^{-3})	1.852
μ (mm^{-1})	1.515
F(000)	3660
θ range (deg)	2.93 - 25.34
index range	$-28 \le h \le 28$, $-28 \le h \le 28$, $-15 \le h \le 15$
measd reflns	14096
indep reflns/R_{int}	2657/0.0313
obsd reflns	2657
$R1^a$ [$I > 2\sigma(I)$]	0.0219
$wR2^b$ (all data)	0.0469
GOF on F^2	1.058
Flack parameter	0.04(2)
$\Delta\rho_{max}/\Delta\rho_{min}$/ (e $Å^{-3}$)	0.391/-0.254

$^a R1 = ||F_o| - |F_c||/|F_o|$. $^b wR2 = [w(F_o^2-F_c^2)^2]/[w(F_o^2)^2]^{1/2}$.
$w = 1/[\delta^2(Fo^2)+(0.0219P)^2+9.5618P]$, $P=(Fo^2+2Fc^2)/3$

Table S2

Selected bond lengths (Å) and bond angles (°) for **1**.

Cd(1)-N(21)#1	2.259(3)	Cd(1)-O(21)	2.311(3)
Cd(1)-N(11)	2.304(3)	Cd(1)-O(12)#2	2.374(3)
Cd(1)-O(11)#2	2.305(3)	Cd(1)-O(22)	2.439(3)
N(21)#1-Cd(1)-N(11)	98.32(11)	N(21)#1-Cd(1)-O(21)	107.22(11)
N(21)#1-Cd(1)-O(11)#2	100.67(11)	N(11)-Cd(1)-O(21)	95.22(10)
N(11)-Cd(1)-O(11)#2	100.54(12)	O(11)#2-Cd(1)-O(21)	145.48(12)
N(21)#1-Cd(1)-O(12)#2	155.81(11)	N(11)-Cd(1)-O(12)#2	91.48(11)
O(11)#2-Cd(1)-O(12)#2	55.61(11)	O(21)-Cd(1)-O(12)#2	93.74(11)
N(21)#1-Cd(1)-O(22)	93.31(11)	N(11)-Cd(1)-O(22)	149.89(10)

O(11)#2-Cd(1)-O(22)	104.47(12)	O(21)-Cd(1)-O(22)	54.73(9)
O(12)#2-Cd(1)-O(22)	89.00(12)	C(16)-O(11)-Cd(1)#3	92.5(2)
C(16)-O(12)-Cd(1)#3	89.4(2)	C(26)-O(21)-Cd(1)	94.1(2)
C(26)-O(22)-Cd(1)	88.1(2)		

Symmetry codes: #1 *x* - 1/3, *x* - *y* + 1/3, *z* - 1/6; #2 *x*, *x* - *y*, *z* + 1/2; #3 *x*, *x* - *y*, *z* - 1/2.

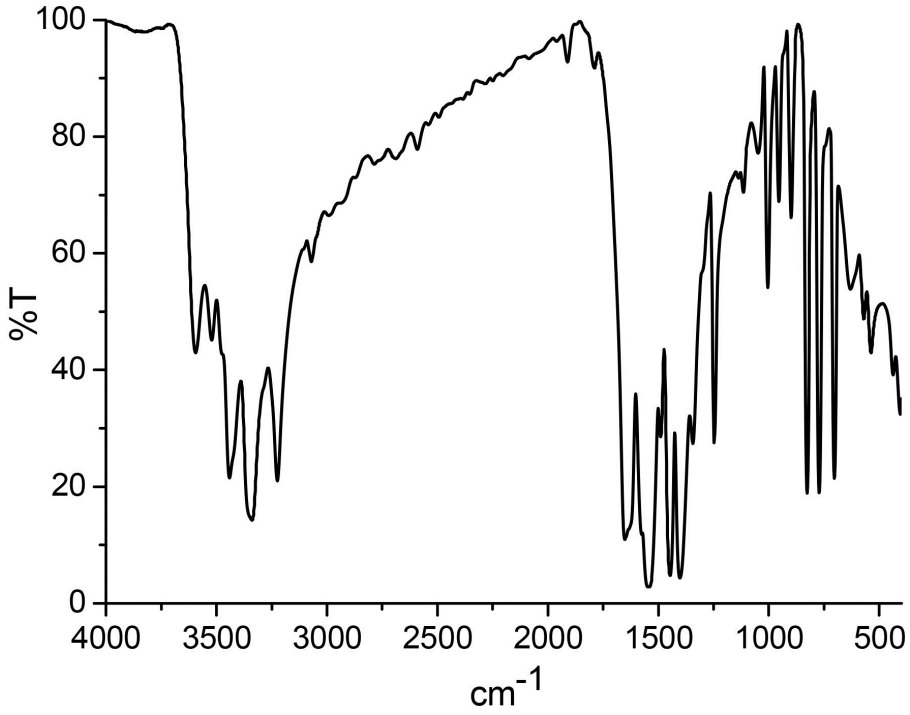

Figure S1. The IR spectrum of **1**.

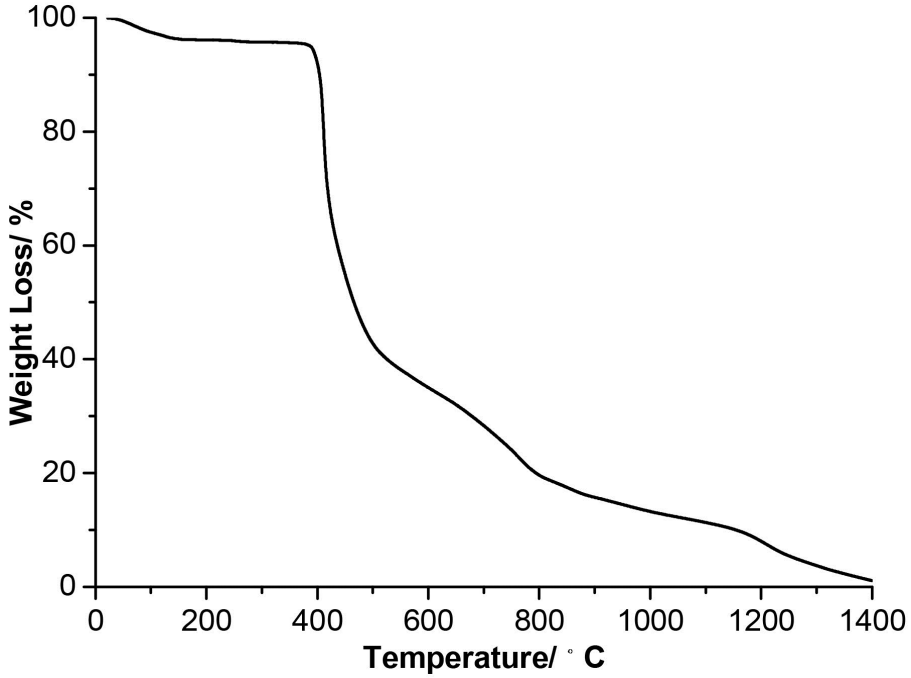

Figure S2. TGA spectrum of **1**.

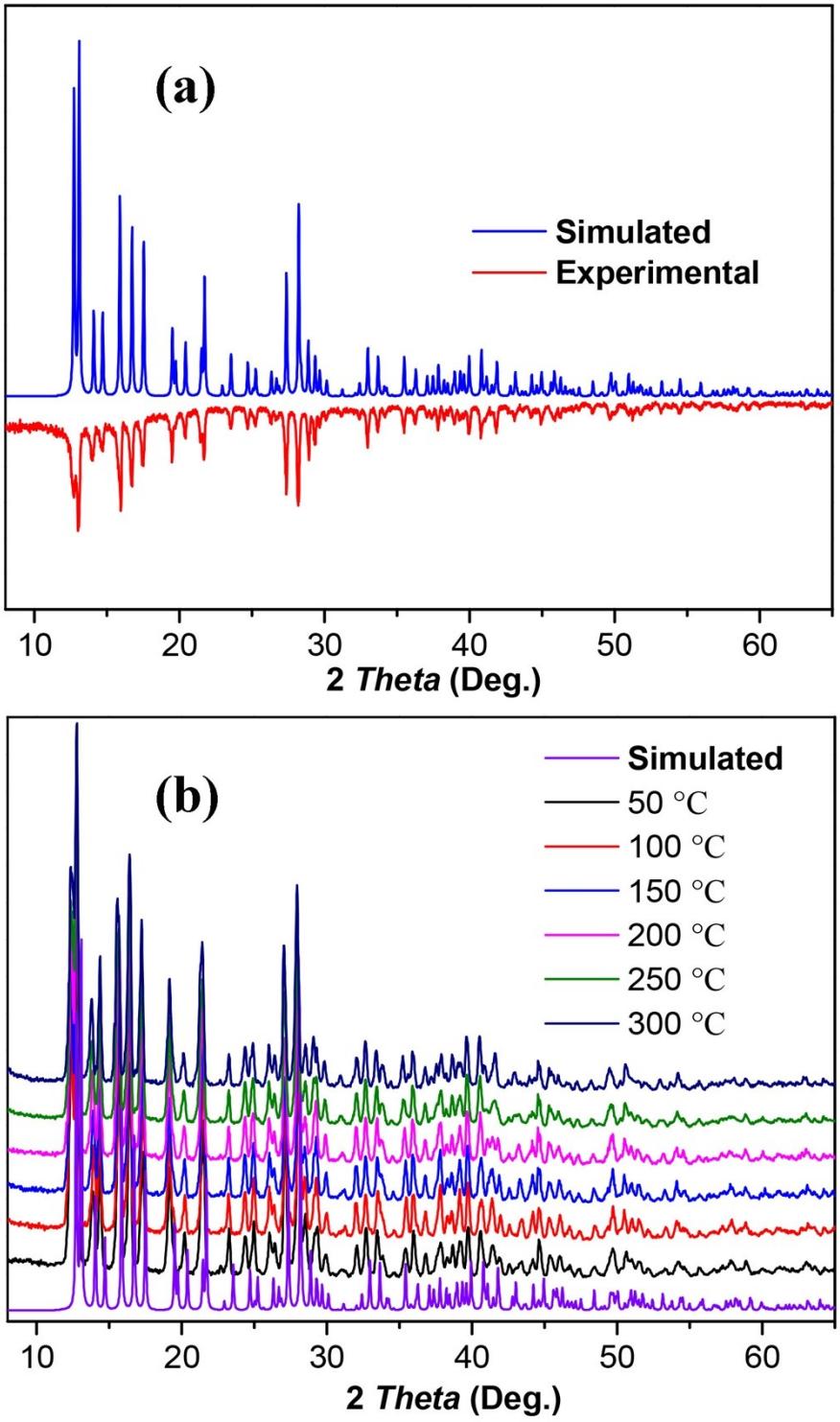

Figure S3. (a) Powder X-ray diffraction profiles of **1**; (b) Temperature-dependent powder X-ray diffraction of **1**.

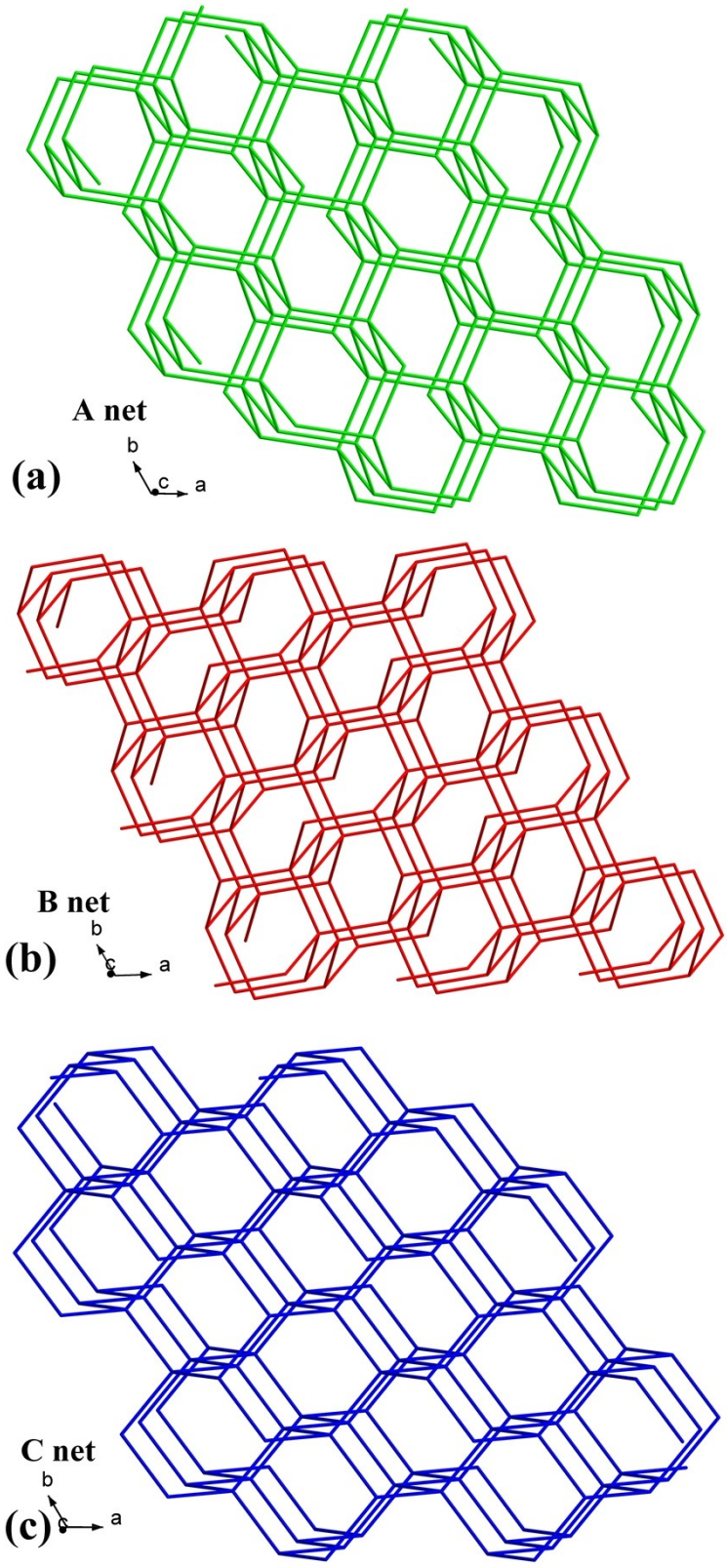

Figure S4. Schematic views of A(a), B(b) and C(c) nets along the *c* axis.

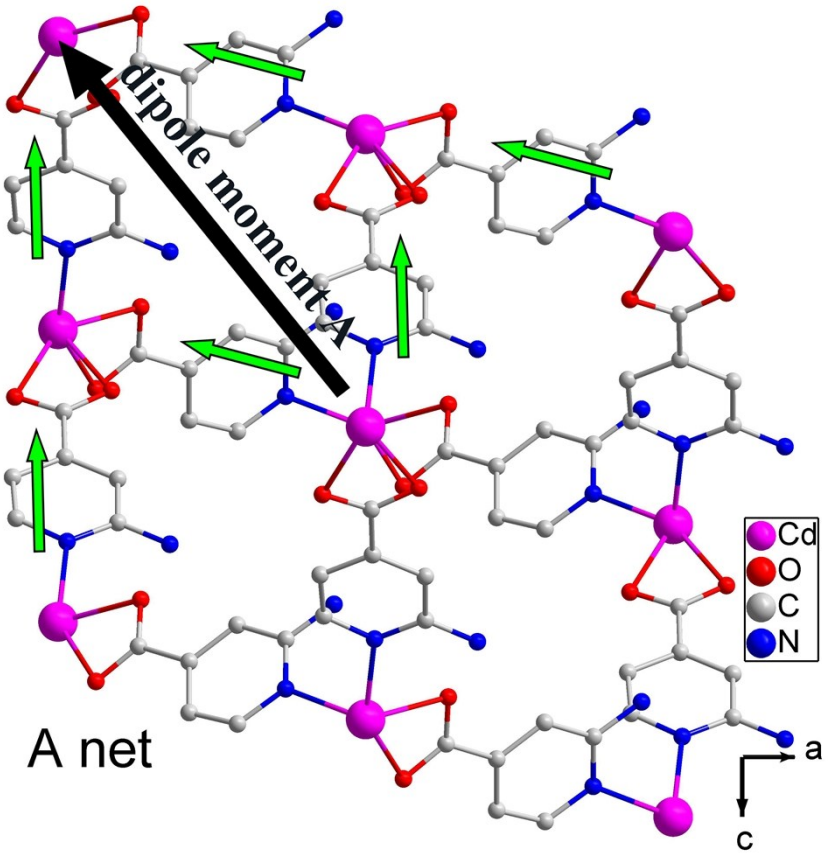

Figure S5. Side view of an adamantanoid cage of A net (green arrows represent dipoles of L2 ligands, the black arrow represents **dipole moment A**).

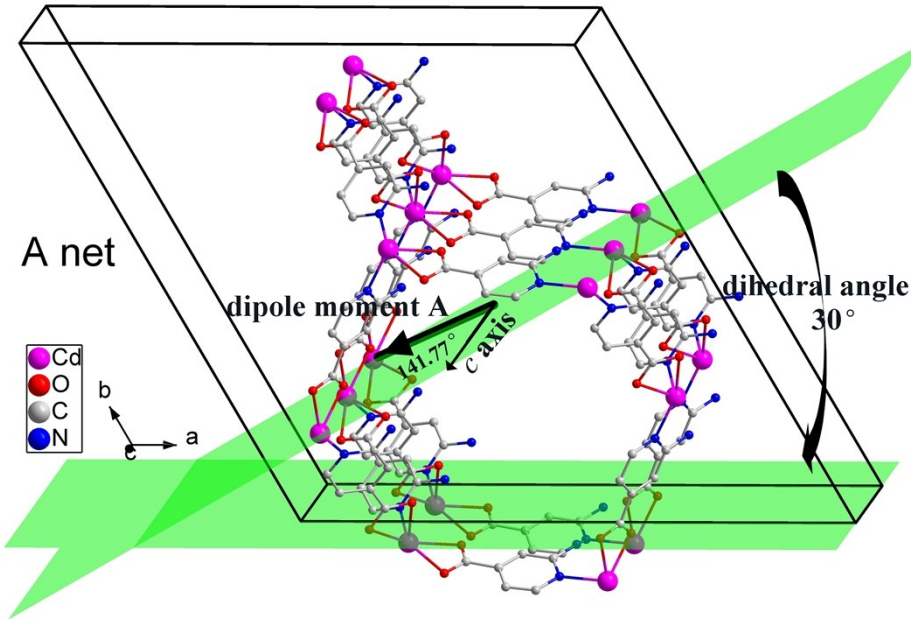

Figure S6. View of the location of **dipole moment A** in the crystal cell along the *c*

axis.

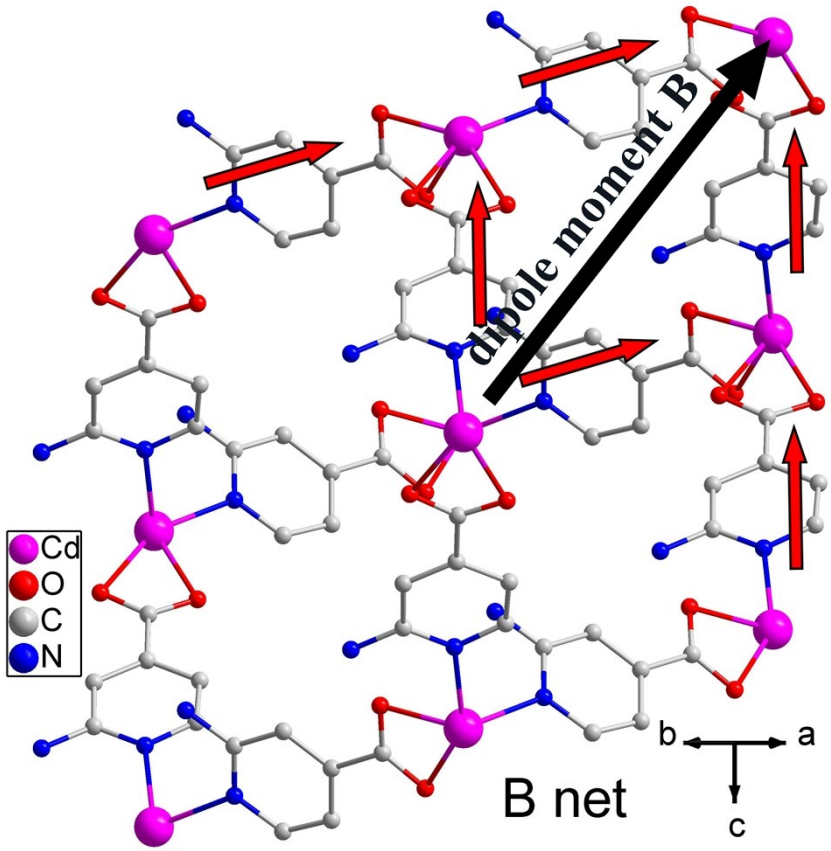

Figure S7. Side view of an adamantanoid cage of B net (red arrows represent dipoles of L2 ligands, the black arrow represents **dipole moment B**).

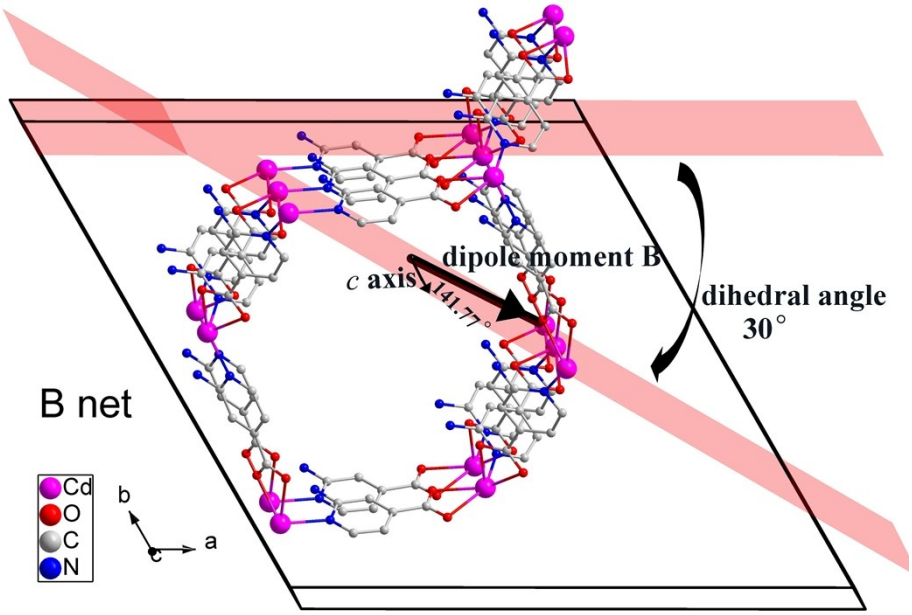

Figure S8. View of the location of **dipole moment B** in the crystal cell along the *c* axis.

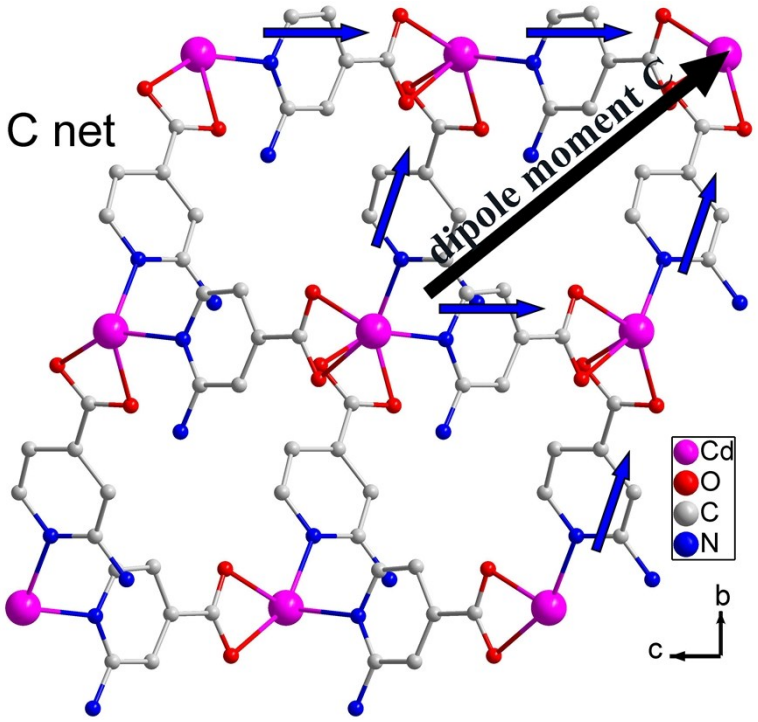

Figure S9. Side view of an adamantanoid cage of C net (blue arrows represent dipoles of L2 ligands, the black arrow represents **dipole moment C**).

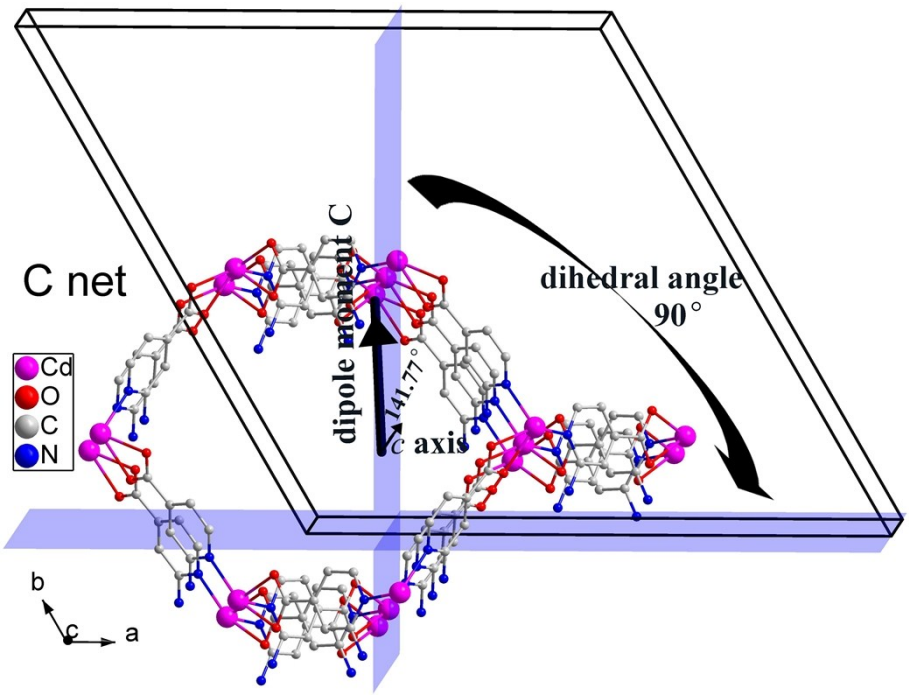

Figure S10. View of the location of **dipole moment C** in the crystal cell along the *c* axis.

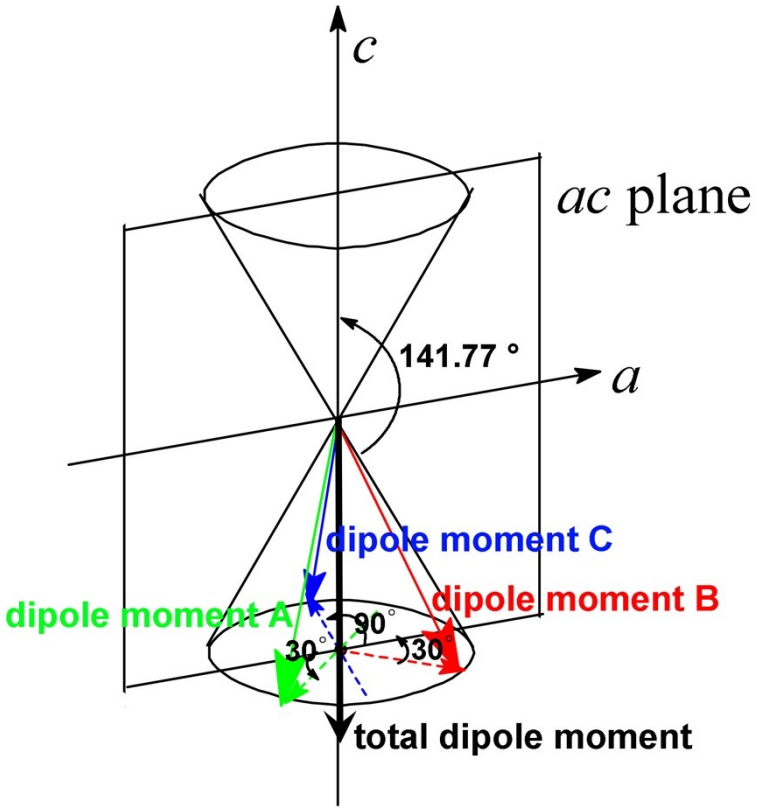

Figure S11. View of the locations of **dipole moments A, B, C** and **total dipole moment** of **1**.

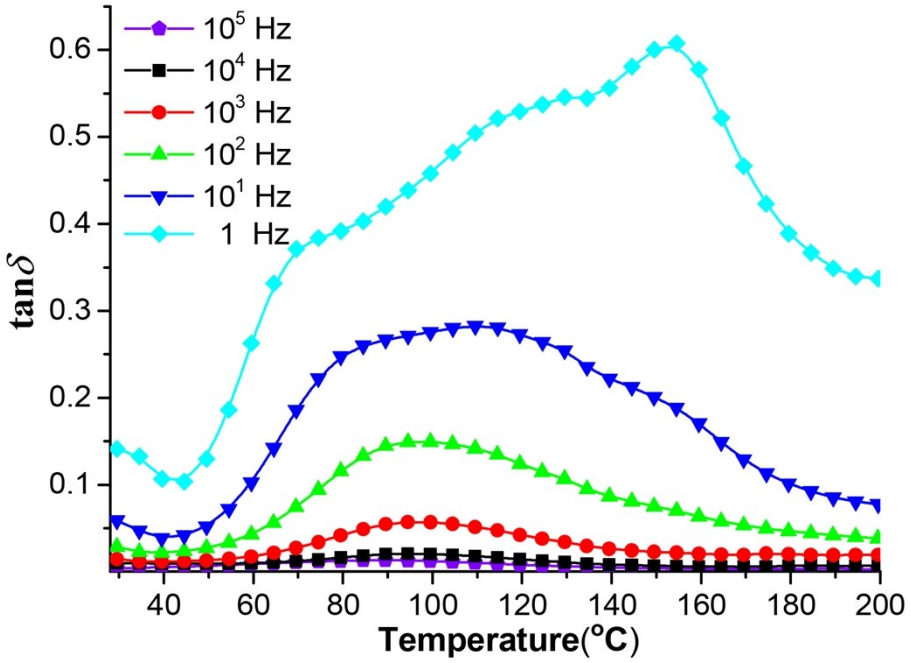

Figure S12. The temperature dependence of the dielectric loss tanδ of **1** at various frequencies between 1 Hz and 100 kHZ.

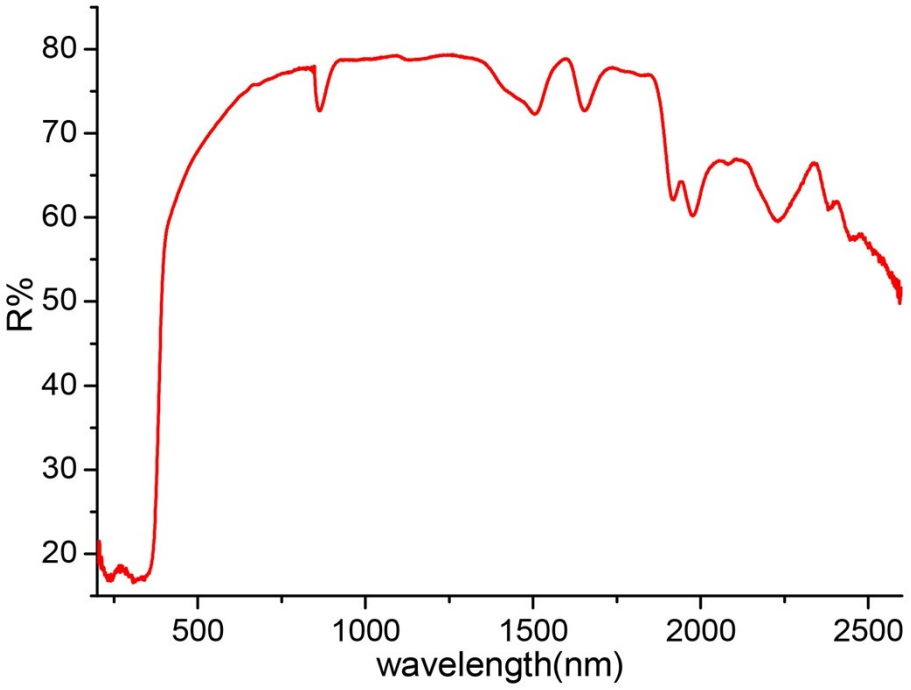

Figure S13. Optical diffuse reflectance spectrum for **1**.

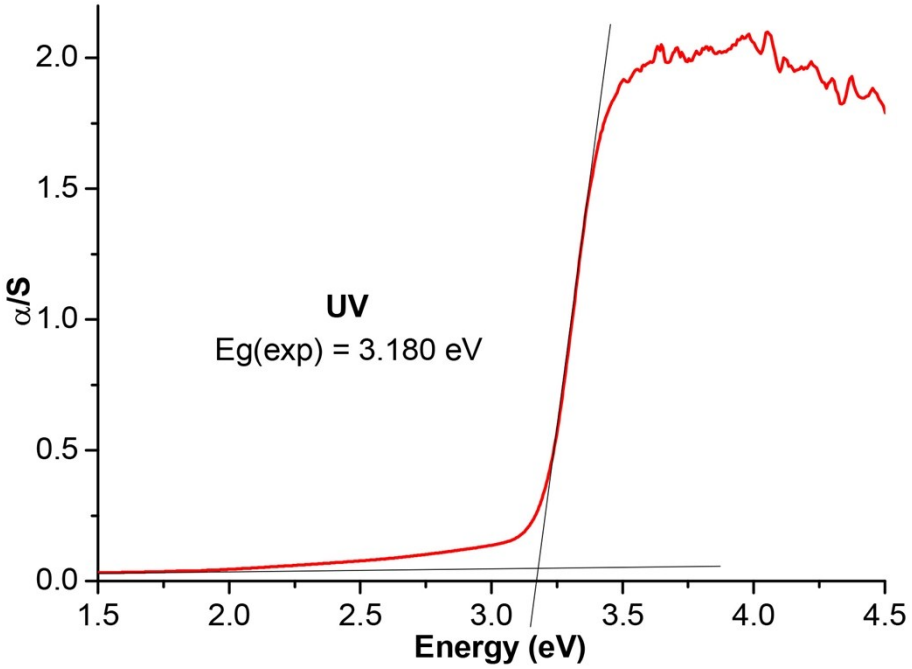

Figure S14. Absorption spectrum of **1**, converted from UV diffuse-reflectance spectrum of **1**.

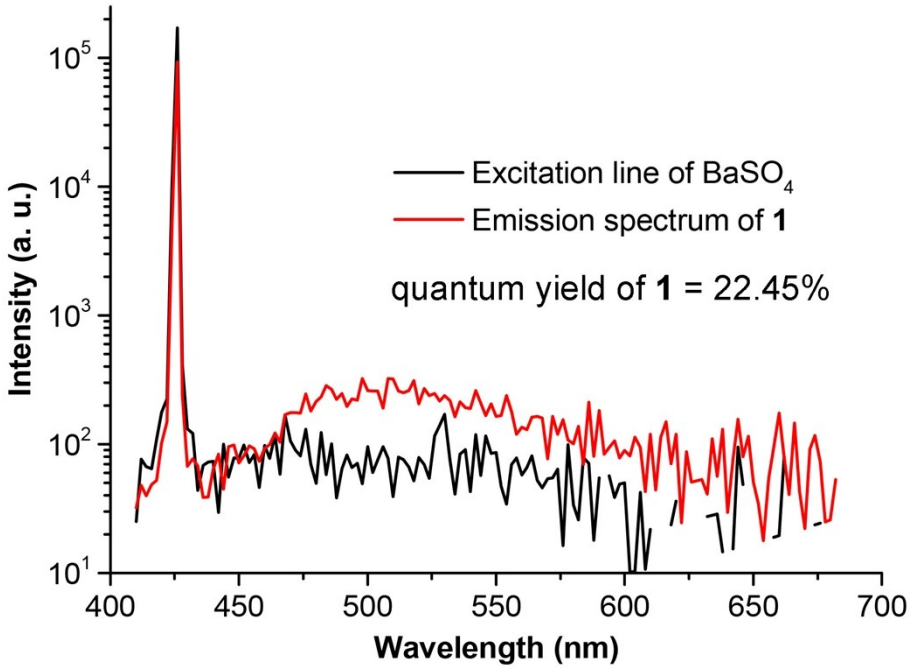

Figure S15. Excitation line of $BaSO_4$ and emission spectrum of **1** by an integrating sphere.

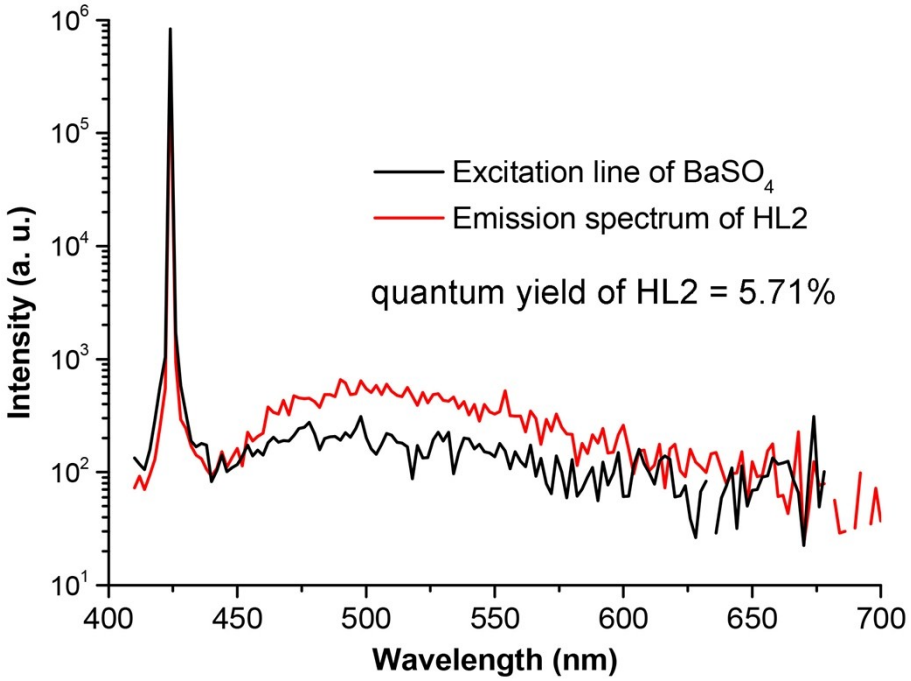

Figure S16. Excitation line of $BaSO_4$ and emission spectrum of HL2 by an integrating sphere.

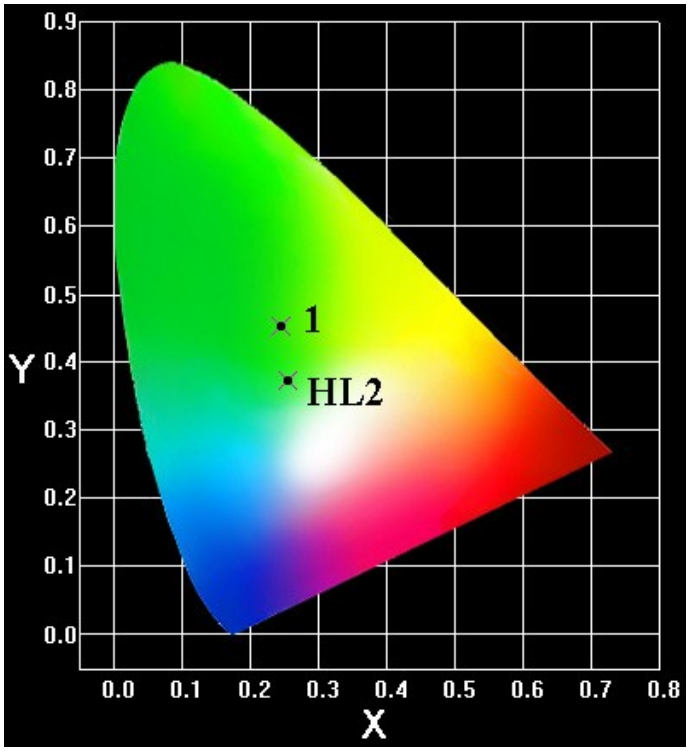

Figure S17. CIE-1931 chromaticity diagram showing the green PL of **1** and HL2.

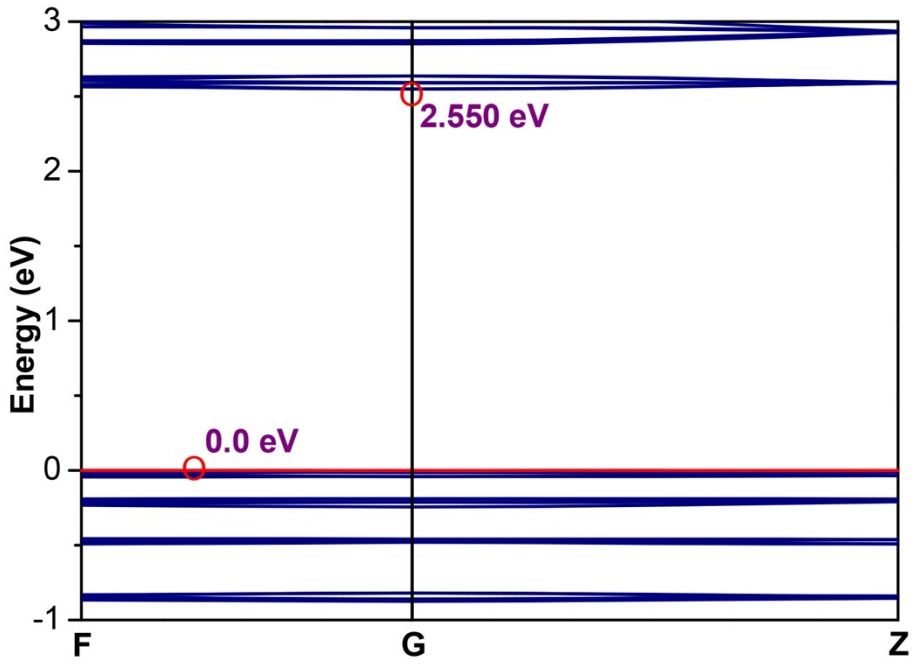

Figure S18. Band structure of **1** (band are shown only between -1.0 and 3.0 eV for clarity, and red line indicates the position of the Fermi level).

---

[i] a) W. W. Wendlandt and H. G. Hecht, Reflectance Spectroscopy; Interscience Publishers: New York, 1966; b) G. Kortüm, Reflectance Spectroscopy; Springer-Verlag: New York, **1969**.

[ii] S.K. Kurtz, T.T. Perry, J. Appl. Phys. 39, **1968**, 3798.

[iii] Siemens, *SHELXTL™ Version 5 Reference Manual*, Siemens Energy & Automation Inc., Madison, Wisconsin, USA, **1994**.